Instrument requirements for precision relative astrometry using TMT/IRIS

Ryuji Suzuki*[a], Hiroki Harakawa[a], Matthias Schöck[b], Brent Ellerbroek[b]
[a]National Astronomical Observatory of Japan, 2-21-1 Osawa, Mitaka, Tokyo, JAPAN; [b]TMT International Observatory, 100 West Walnut Street, Suite 300, Pasadena, CA, USA

ABSTRACT

InfraRed Imaging Spectrograph (IRIS) is one of the three instruments that will be available at the first light of TMT. Working with the facility adaptive optics system NFIRAOS, IRIS provides diffraction limited imaging and integral field spectroscopic capabilities in the near-infrared wavelength range. One of the unique observing performances of IRIS is precision relative astrometry at a level of 30 uas. Achieving this un-precedented accuracy necessitates a number of contributing error terms, including target property errors, atmospheric property errors, AO performance errors, opto-mechanical errors, detector characteristic errors, and data reduction errors, to be reduced by design, calibration, operation, and data reduction. We have created a detailed astrometry error budget which identifies all error terms, quantifies them, and distributes allocations to individual terms to enable the required astrometry accuracy. This error budget is written in terms of astrometric accuracy, i.e., uas, and each error term needs to be translated to technical languages through analyses and simulations when it flows down to system and subsystem requirements. This paper describes the analyses and simulations that we have done to derive the requirements for IRIS with a focus on atmospheric dispersion, optical distortion, and detector characteristics.

Keywords: TMT, IRIS, astrometry, requirements

1. INTRODUCTION

InfraRed Imaging Spectrograph (IRIS; Larkin et al. 2016)[1] is one of the first light instruments of the Thirty Meter Telescope, which is under construction due for completion in late 2020s. IRIS will provide diffraction limited imaging and integral field spectroscopic capabilities in the near infrared wavelength range with the help of the facility Adaptive Optics system NFIRAOS (Herriot et al. 2014)[2]. One of the unique observing capabilities of IRIS is precision relative astrometry. With the extremely large aperture of the telescope and excellent image quality delivered by NFIRAOS, IRIS will enable the highest precision astrometry ever at the level of 30 micro-arcsec (uas). AO assisted infrared instruments currently on board 8-10 m class telescopes have achieved astrometric error of ~ 150 uas, limited by the optical distortion correction error, field dependent PSF uniformity, and time dependent PSF stability (Fritz et al. 2009[3]; Yelda et al. 2010[4]). All three errors are expected to be greatly improved by NFIRAOS which employs the multi-conjugate adaptive optics architecture because of superior wavefront correction performance over the IRIS field (34" x 34") using two deformable mirrors and six laser guide stars, a stable temperature environment, and the use of on-instrument wavefront sensors to stabilize the telescope plate scale change (breathing) and resulting distortion pattern change. It is, however, still challenging enough to achieve the astrometric accuracy of ~ 30 uas since many error sources come up to surface which have not been visible with the previous accuracy. They include target property errors, atmospheric property errors, AO performance errors, opto-mechanical errors, detector characteristic errors, and data reduction errors. In order to achieve the astrometric accuracy of ~ 30 uas, they have to be properly reduced by design, calibration, operation, and data reduction. TMT formed an astrometry working group with members from the telescope system, NFIRAOS, IRIS, and astronomers to identify all error terms, quantify them, and create a plan to achieve our astrometry goals. The outcome of our efforts has been published as the TMT astrometry error budget (Schöck et al. 2014)[5]. The astrometry error budget distributes allocations to individual error terms in the unit of "uas". The individual allocations need to be flow down to system, subsystem, and all the way to component levels through proper budgeting, calibration plan, operation plan, data reduction plan, and associated supporting analyses (Schöck et al. 2016)[6]. This paper describes the analyses specifically related to residual atmospheric dispersion, optical distortion, and detector characteristics. We aim to derive requirements which guide instrument design, fabrication, calibration plan, operation plan, observation plan, and data reduction plan.

The structure of this paper is as follows. We describe and formulate the various classes of data used in each analysis in Section 2. Section 3 summarizes various requirements derived from the analyses with brief descriptions and notes for some results.

2. METHOD AND DATA

2.1 Object position in presence of spectral dispersion

The observed position of a star in an image ($\vec{Y}$) in presence of spectral dispersion in the light path can be expressed as,

$$\vec{Y} = \vec{Y}_0 + \frac{\int \vec{D}_{(\lambda)} F_{p(\lambda)} T_{(\lambda)} d\lambda}{\int F_{p(\lambda)} T_{(\lambda)} d\lambda} \quad (1)$$

where $\vec{D}_{(\lambda)}$ is the spectral dispersion in the light path, $T_{(\lambda)}$ is a throughput profile, and $F_{p(\lambda)}$ is the Spectral Energy Distribution (SED) of the star in terms of photon flux. $\vec{Y}_0$ is the position when the spectral dispersion is zero. The object position can be corrected in the post analysis, using the estimated objects' spectral information (e.g., SED, color), throughput profile, and dispersion profile. The corrected object position ($\vec{Y}'$) is written as,

$$\vec{Y}' = \vec{Y} - \vec{\hat{Y}} \quad (2)$$

$$\vec{\hat{Y}} = \frac{\int \vec{\hat{D}}_{(\lambda)} \hat{F}_{p(\lambda)} \hat{T}_{(\lambda)} d\lambda}{\int \hat{F}_{p(\lambda)} \hat{T}_{(\lambda)} d\lambda} \quad (3)$$

where variables with "hat" represent estimated quantities. The correction accuracy, and hence the astrometric accuracy, depends on the level of accuracy of our knowledge about the objects' SED, throughput profile, and dispersion profile in the light path. The three error categories are broken down to specific error sources below.

- SED
  - Diversity of SEDs
  - Quality of spectra
  - Color error
- Throughput profile
  - Atmospheric transmission
  - Instrument transmission
  - Filter coverage
- Dispersion profile
  - Residual atmospheric dispersion

We investigate how individual errors listed above propagate to the astrometric error through simulations outlined in the following sections.

2.1.1 Diversity of SEDs

We use observed and theoretical spectra from Rayner et al. (2009)[7] and Kurucz (1993)[8], respectively, as SED templates for various types of stars. Rayner et al. (2009) provide observed spectra of F to M stars with R ~ 2,000 from 0.8 to 2.5 microns. A total of 135 spectra with -1.2 < J-K < 1 are chosen for this analysis from spectra which do not suffer from extinction. Kurucz (1993) calculated theoretical spectra with a wide range of physical parameters and various models. We use their ODFNEW model with the following physical parameters.

- Effective temperature: 3,500 – 50,000 K
- Surface gravity: 2 – 5
- Metallicity: -2.0 - +0.5 $[M/H]_{sun}$

- Turbulence velocity: 0, 2
- Mixing parameter: 1.25

For convenience of discussion, the theoretical spectra are classified as O to M stars by the effective temperatures. We chose 30 objects for each spectral type in order to reduce the computation load while keeping the meaningful results out of the analysis. The numbers of objects used in this paper are summarized in Table 1.

Table 1. The number of objects per spectral type used in the analyses.

	O	B	A	F	G	K	M
Rayner et al. (2009)	-	-	-	31	26	20	43
Kurucz (1993)	30	30	30	30	30	30	30

2.1.2 Quality of spectra

To see how the quality of spectra (i.e., signal-to-noise ratio and spectral resolution) affects the astrometric accuracy, we first create noise-free spectra which represent ideal measurements. Ten objects ranging from F to M stars are chosen from Rayner et al. (2009), and each SED is fit with a function of form,

$$\log f_{(\lambda)} = \sum_i p_i e^{-\frac{(\lambda-\lambda_i)^2}{\sigma_i^2}} + \sum_j \sum_k q_{jk}\lambda^k, \quad (4)$$

where

$\sigma_i = \sigma_{i,b}$ for $\lambda < \lambda_i$

$\sigma_i = \sigma_{i,a}$ for $\lambda \geq \lambda_i$

The first term introduces line absorptions of Gaussian form, while the second polynomial term ($\sum_j \sum_k q_{jk}\lambda^k$) represents a continuum spectrum. The absorption line with a peak depth of p_i has two different widths ($\sigma_{i,b}$ and $\sigma_{i,a}$) before and after the center wavelength to represent an asymmetric absorption profile seen in the CO absorption band. The number of polynomials (j) and the number of polynomial terms (k) are typically 1-2 and 1-3, respectively, while the number of absorption lines (i) depend on the spectrum. We add Gaussian noise to the spectra to simulate various signal-to-noise ratios, and apply a box filter of various box sizes to reduce spectral resolutions ($R = \lambda/\Delta\lambda$).

For each combination of spectral resolutions (R=2,000, R=1,000, R=500, and R=100) and signal-to-noise ratios (S/N=infinity, S/N=100, S/N=10, S/N=3), one hundred spectra are created with different noise realizations. The object position is calculated for each spectrum, and the deviation from the one with R=2,000 and S/N=infinity is combined for all ten objects.

2.1.3 Color error

Color is the lowest spectral resolution quantity that can be used to estimate the SED. If only the object color is available but not the SED, the object position estimate and the object color (X) can be related by a polynomial below,

$$\left|\vec{\hat{Y}}\right| = \sum_i a_i X^i \quad (5)$$

$$X = \frac{\int F_{e(\lambda)} T_{1(\lambda)} d\lambda}{\int F_{e(\lambda)} T_{2(\lambda)} d\lambda} \quad (6)$$

where, $F_{e(\lambda)}$ is the SED of the star in terms of energy flux, and T_1 and T_2 denote throughput profiles of the two filters used. The object position $\left|\vec{\hat{Y}}\right|$ and the color X are calculated for a variety of SEDs described in Section 2.1.1 together with the dispersion and transmission estimates. Then the coefficients ($\boldsymbol{a_i}$) are derived by the least square fitting of Eq. (5) to $\left|\vec{\hat{Y}}\right|$ and X. Finally, the error propagation can be written as,

$$\sigma^2_{\left|\vec{\hat{Y}}\right|} = \left(\frac{\partial\left|\vec{\hat{Y}}\right|}{\partial X}\right)^2 \sigma_X^2 + \sigma_r^2 \quad (7)$$

where σ_r is a standard deviation of data points from Eq. (5).

2.1.4 Atmospheric transmission

Atmospheric transmission profiles of a model atmosphere under various water vapor and airmass conditions are available from Gemini North Observatory (https://www.gemini.edu/sciops/telescopes-and-sites/observing-condition-constraints/ir-transmission-spectra). We use the model for Mauna Kea where TMT is planned to be built.

2.1.5 Instrument transmission

Modeling an instrument throughput profile for general cases is quite difficult, but it is reasonable to represent the profile as a combination of two features; (1) cut-on, cut-off wavelengths defined by bandpass filters, and (2) periodic throughput variation (ripple) of the optical coatings in the transparent wavelength range. Both features are subject to calibration errors and temperature error because they have a temperature dependency. We model the transmission curve of the latter case as follows.

$$T_{(\lambda)} = T_0 + A\sin\left(2\pi\frac{\lambda-\lambda_{on}}{\lambda_{off}-\lambda_{on}}n + \theta\right) \qquad \lambda_{on} \le \lambda \le \lambda_{off} \tag{8}$$

$$T_{(\lambda)} = 0 \quad \lambda \le \lambda_{on} \text{ or } \lambda \ge \lambda_{off} \tag{9}$$

where T_0 is the average transmission, A is the amplitude of the transmission ripple, λ_{on}, λ_{off} are the cut-on and cut-off wavelengths, n is the number of cycles of the ripple, and θ is the phase shift of the ripple. T_0 and A only matter in the form of A/T_0 since the average transmission itself does not change the object position. θ is randomly given in $0 < \theta \le 2\pi$, although it is expected to be very small in reality.

2.1.6 Filter coverage

Use of narrowband filter is an obvious choice for reducing the astrometric error since the residual atmospheric dispersion becomes smaller in the narrower filter coverage. One possible drawback of using a narrowband filter may be loss of observing sensitivity. In the background limited observing conditions, the observing sensitivity, which is the inverse of the exposure time (t) necessary to achieve certain signal-to-noise ratio, can be approximated as

$$\frac{1}{t} \propto \frac{\int f_{obj} T d\lambda}{\int f_{bg} T d\lambda} \tag{10}$$

where f_{obj} is the object's SED, f_{bg} is the sky and telescope background profile, T is the transmission profile in the light path. We investigate how the astrometric error and the observing sensitivity change as we change the center wavelength and coverage of the filters to identify suitable filters for precision astrometry with high observing efficiency.

2.1.7 Residual atmospheric dispersion

Atmospheric dispersion is on the order of ~15 - 80 mas in the coverage of individual NIR broadband filters. It can be compensated to a few mas or less using an Atmospheric Dispersion Corrector (ADC) (see Phillips et al. 2010 for IRIS)[9]. The residual atmospheric dispersion contributes to the astrometric error in two ways. The nominal residual atmospheric dispersion ($\vec{D}_{(\lambda)}$) is coupled with other error terms, while its error also propagates to the astrometric error. There are three error terms in the residual atmospheric dispersion; (1) the residual associated with fabrication, calibration, and operation error of the ADC, (2) the residual related to the atmospheric conditions, e.g., varying temperature, pressure, and humidity, and (3) the residual originating from errors in the atmospheric model. We assume that the nominal residual atmospheric dispersion within individual filter coverage has a quadratic form with wavelength which is symmetric about the center wavelength. We also assume that the residual atmospheric dispersion error within an individual filter's coverage is represented by a slope or a quadratic function of wavelength. We believe that the assumptions are reasonable since the residual and its error are small compared to the atmospheric dispersion.

2.2 Optical distortion

NFIRAOS and IRIS are required to characterize the optical distortion at an accuracy of 8 uas. In many astronomical instruments in the past, the optical distortion has been calibrated against a reference object whose position is known accurately *a priori*. However, this "reference method" is not feasible in our case due to unprecedented accuracy required (i.e., there is no reference object whose position is known to ~ 8 uas, or 17 nm in the telescope focal plane). We instead decide to adopt a "self-calibration method" to calibrate the optical distortion to an unprecedented regime using a pinhole grid mask and XY stages deployed in the telescope focal plane in NFIRAOS. The pinhole grid mask is dithered in the telescope focal plane, and the distortion pattern is extracted from the pinhole coordinates measured by IRIS at different

dither positions. Details of the distortion calibration plan, algorithm, and simulation results are beyond the scope of this paper. They are given in a dedicated technical document[10] (Suzuki 2017).

2.3 Detector characteristics

Detector characteristics need to be understood well in order to achieve an astrometric accuracy of ~ 30 uas since this is less than one hundredth of the pixel scale of IRIS (4 mas). We investigate two detector characteristic errors in this paper; intra-pixel sensitivity (IPS) and pixel-size irregularity (PSI).

2.3.1 Intra-pixel sensitivity

Hardy et al. (2015)[11] investigated the intra-pixel response of the Hawaii1-RG array for the Faint Guide Star camera on JWST. They found that the largest response variation can be attributed to charge diffusion within the bulk detector materials, while multiple sensitivity holes were observed in ~ 10 % of the pixels. We focus on the sensitivity holes in this paper, because the charge diffusion is uniform among all pixels.

The pixel value after flat field correction can be written as,

$$N_i = \frac{\int_{x_i}^{x_{i+1}} f_{(x)} s_{(x)} dx}{\int_{x_i}^{x_{i+1}} s_{(x)} dx}, \tag{11}$$

where $f_{(x)}$ is the flux distribution of the stellar image, and $s_{(x)}$ is the sensitivity profile. In the regime where the IPS is small enough (i.e., $s_{(x)}$ ~ const), the pixel value exactly represents the stellar flux distribution. If there is a "hole" of sensitivity at the position where the stellar flux illuminates the detector, it causes a systematic error of the pixel value, which depends on the slope of the flux distribution even after flat fielding correction for each pixel has been applied.

We assume that the sensitivity hole is represented by a Gaussian function with FWHM of 0.2 pix which is visually deduced from the results in Hardy et al. (2015). We also assume, as the worst case scenario, that the sensitivity hole is completely dark ($s_{(x)}$ = 0) at its peak. A high resolution flat fielding image of the sensitivity hole is created using 10 x 10 subpixels per IRIS pixel. We use a simulated diffraction-limited PSF of TMT at 2.20 um, and extract a central 20 x 20 pixel area (PSF-1). The PSF is upsampled by a factor of 10 using 2-D cubic spline interpolation to be compatible with the high resolution flat fielding image, and it is downsampled back to the original resolution using Eq. (11) (PSF-2; right panel of Figure 1). The left and middle panels of Figure 1 show the sensitivity maps with the sensitivity hole at high and original resolution, respectively. The object position is calculated by 2-D cross-correlation between PSF-1 and PSF-2. We repeat this process while moving the position of the sinsitivity hole from the center of the PSF to the edge of the image.

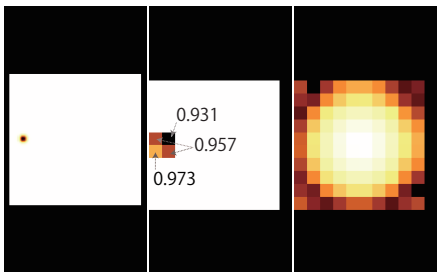

Figure 1. Sensitivity map with the sensitivity hole at 10 times higher resolution than IRIS pixel resolution (left). The same sensitivity map at IRIS pixel resolution (middle). PSF image after flat fielding correction (right; PSF-2)

2.3.2 Pixel size irregularity

Pixel size is not perfectly uniform due to imperfections in the lithgraphic process including patterning, deposition, etching, and doping, etc. It is difficult to generalize and formulate properties of the irregularity because they really depend on the process which detector vendors adopt. We assume in this paper that each pixel has a uniformly random error in its size. We believe that this is close to the worst case scenario, because some errors may follow a Gaussian distributions and there should be contributions from systematic errors which may be corrected by the distortion correction process as we describe later.

Because of pixel continuity, the effect of PSI is not on a pixel by pixel basis, but it is cumulative, e.g., PSI of the 10th pixel affects the pixel position of the 100th pixel. The PSI can be regarded as a non-linearity of a physical pixel position against a regularly gridded pixel index. It therefore has the same effect as the optical distortion and it is in fact subject to the optical distortion correction. The optical distortion correction using a pinhole grid described in Section 2.2 can correct the distortion up to a spatial frequency which corresponds to the pinhole grid interval (f_0). The distortion correction error can be estimated by integrating the power spectral density (PSD) of the distortion profile at frequencies higher than f_0. We simulate a 4K x 4K pixels detector with PSI for a variety of amplitudes ranging from 0.1 – 10 % of the pixel size. An average PSD from one thousand simulations is fit by an offset power law of form,

$$PSD_{(f)} = \alpha f^{\beta} + \gamma \tag{12}$$

If the astrometric error allocated to PSI is σ_{PSI}, then the required pinhole grid interval can be calculated by the following equation.

$$\int_{f_0}^{1} PSD_{(f)} df = \sigma_{PSI}^2 \tag{13}$$

3. RESULTS

Table 2 shows a summary of requirements derived through the analyses outlined in the previous section. We will give discussions and notes for some results in the following sub-sections. It should be noted that individual requirements cannot be derived by themselves, but only through balancing allocations among all error contributors in the error budget. The requirements shown here may be somewhat arbitrary (i.e., some requirements may be tighter than the others) because no optimization is performed for technical difficulty of the error contributors in the error budget. It should also be noted that the requirements are subject to change in the future as the instrument design matures.

Table 2. Summary of requirements derived in this paper.

Item	Requirement
SED	
SED	Object SED is necessary for stars later than G stars.
Quality of SED	R > 100 and S/N > 100
Color error	Shall be less than 0.1 mag for stars earlier than F stars.
Instrument transmission	
Cut-on/off wavelength	Shall be known to 100 A at operating temperature and at any field position.
Transmission profile	Shall be known to 1% of the peak transmission within a filter coverage.
Narrowband filter	See Table 3
Atmospheric transmission	
Atmospheric transmission	Negligible effect (no requirement)
Residual atmospheric dispersion	
Nominal residual atmospheric dispersion	Shall be smaller than 1 mas peak-to-peak within a filter coverage Shall be calibrated to 0.2 mas
ADC control accuracy	Residual dispersion shall be less than 0.2 mas
Environment monitoring accuracy	Temperature : < 0.6 K Pressure : < 1.2 hPa (See text)
Distortion correction	
Pinhole grid interval	33 x 33 pinholes within a single detector coverage
Measurement error of the pinhole images	Shall be better than 5 uas
Position angle repeatability	Shall be better than 0.0023 deg
Dither length	Shall be larger than 200 pix
A priori knowledge of the pinhole position	Shall be better than 10 um
Detector characteristics	
Intra-pixel sensitivity	We will consult with the detector vendor.
Pixel size irregularity	Shall be less than 0.1 % of pixel size

3.1 Diversity of SEDs

Figure 2 plots the colors and object positions of all the spectra introduced in Section 2.1.1 for K band, as an example, when there is a 1 mas nominal residual atmospheric dispersion in a quadratic form in the filter coverage. This diagram, which we hereafter call "color position diagram" is a convenient tool for visualizing a trend between the object position and color which is a good representation of the spectral type. The color position diagram shows that object positions of our data have a good coincidence with the blackbody sequence in J-band, but they depart from the blackbody sequence from G stars in H-band, and from K stars in K-band. The object positions also scatter more than 10 uas for M stars in all three filter coverages. The right panel of Figure 2 compares the blackbody SEDs with observed SEDs from Rayner et al. (2009). We see that the observed SEDs are not represented by the blackbody SEDs for late type stars due to local spectral features such as water and CO absorption bands. Our results with realistic SEDs show that the object position needs to be corrected using the object's SED for stars later than G stars in order to achieve astrometry at the 10 uas level.

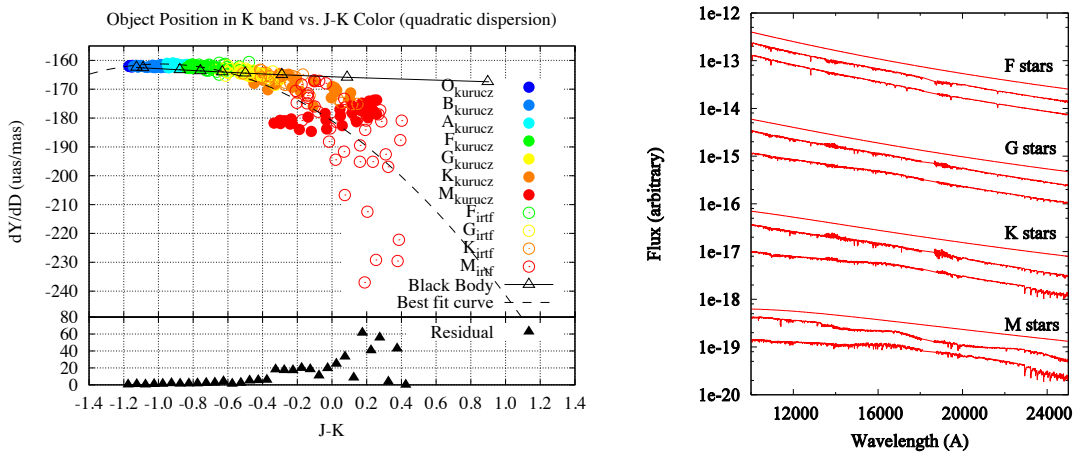

Figure 2. *Left:* Color-position diagram showing a derivative of object position with respect to dispersion amplitude (dY/dD) in K-band as a function of J-K color. Filled and open circles represent data from Kurucz (1993) and Rayner et al. (2009), respectively. The dashed line is the best fit quadratic curve to the data. The bottom plot shows residuals of data points from the best fit curve. The solid line represents a sequence of blackbody SEDs with various effective temperatures. Right: Comparison of typical SEDs of F to M stars from Rayner et al. (2009) with blackbody SEDs of equivalent effective temperatures. The lower two spectra for each spectral type are from Rayner et al. (2009), while the blackbody SED is on the top. Note that the vertical axis has an arbitrary unit.

3.2 Color Error

Figure 3 plots the maximum color error allowed for various astrometric error criteria (represented by solid lines) as a function of J-K color. The plot is specifically for K-band as a representative of the worst case. The standard deviation of the object positions (labeled as residual on the right axis) for each J-K color is represented by filled circles. As we discussed in Section 3.1, the object SED is necessary for stars later than G stars due to increasing deviation from the blackbody sequence and increasing scatters. We set the color error be smaller than 0.1 mas for stars earlier than F stars or J-K < -0.5, which corresponds to ~ 2 uas error.

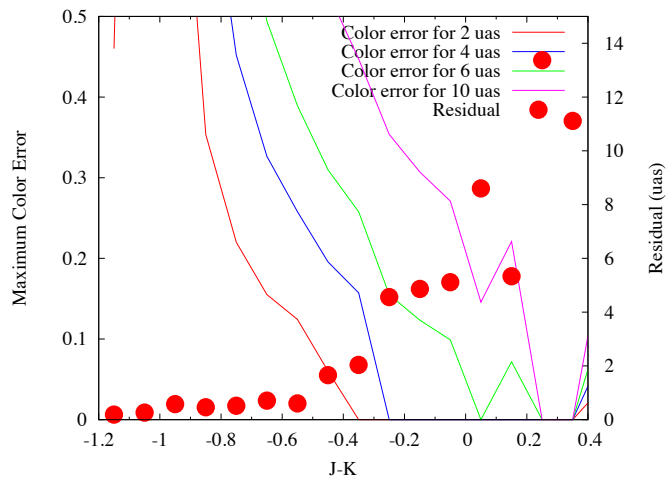

Figure 3. Maximum color error allowed as a function of object's J-K color. Solid lines with different colors denote the maximum color error allowed to achieve the astrometric error of 2 – 10 uas. Filled circles plot a standard deviation of the residuals in the color-object diagram in Figure 2 (scale on the right axis).

3.3 Residual atmospheric dispersion

For the effect of the dispersion to be less than 10 uas, we must characterize the residual atmospheric dispersion of a quadratic form to better than 0.2 mas. We must also control the ADC and monitor atmospheric temperature and pressure to keep the slope of the residual atmospheric dispersion within 0.2 mas. This corresponds to a change in atmospheric temperature of 0.6 K and pressure of 1.2 hPa in J band, 1 K and 2.4 hPa in H band, and 2 K and 4 hPa in K band, respectively. The temperature and pressure can be monitored with better accuracy than the numbers above using commercially available equipment. However, the location of the monitoring point needs to be addressed through measurements of atmospheric dispersion. The atmospheric dispersion at Mauna Kea measured by the AO assisted NIR spectrograph (IRCS) on the Subaru Telescope is consistent with the atmosphere model by Hohenkerk and Sinclair (1985)[12] with 1-3 mas accuracy, largely limited by AO performance (Suzuki et al. 2014)[13]. As they pointed out, the measurement accuracy will be greatly improved using higher order AO in the future, such as NFIRAOS. In fact, IRIS has a parallel observing capability between the imager and the spectrograph. Measuring the atmospheric dispersion with the spectrograph at the same time as doing astrometry in the imager will enable us to achieve the best astrometric accuracy ever and could play an important role for precision relative astrometry using AO assisted instruments.

3.4 Instrument transmission

We found that an error in the cut-on/off wavelength as well as the transmission profile within the filter coverage could affect astrometry at the 10 uas level. We specify requirements that the cut-on/off wavelength of a filter and the transmission profile within the filter coverage shall be calibrated to 100 A and 1 %, respectively, at the operating temperature at any field position.

3.5 Filter coverage

Table 3 lists the center wavelengths and band widths of narrowband filters along with astrometric error and observing sensitivity gain against observation with a broadband filter. Sensitivity gain of more than 1 means that less exposure time is necessary to achieve the same signal-to-noise ratio as the broadband filter observations. All narrowband filters fit in gaps between OH emission lines where the background is low. It should be noted that the filter transmission profile is assumed to be a square profile with a peak transmission of 1, and generally the narrower band width filter is harder to make and the peak transmission is lower.

Table 3. List of narrowband filters which enable precision astrometry with high observing sensitivity

Center wavelength (A)	Band width (A)	Astrometric error (uas)	Sensitivity	Center wavelength (A)	Band width (A)	Astrometric error (uas)	Sensitivity
11880	180	2.5	1.2	17590	100	0.3	0.65
21420	160	0.4	0.91	14970	60	0.5	0.69
20800	100	0.2	2.5	14990	100	0.7	0.92
11760	200	3.4	2.3	15770	120	0.7	1.24

3.6 Optical distortion

A set of requirements is derived for the pinhole grid, XY stages, and measurement accuracy of the pinholes in the IRIS images. It should be noted that the requirements for the pinhole and XY stages are somewhat different from what the self-calibration method generally requires, due to a limitation specific to our case. For example, a large dither length, not exceeding half the detector width, is generally preferred because it produces large differential distortion which can be easily distinguished from the measurement error. In our case, we cannot dither a large distance because of limited space around the telescope focal plane. Another example is that the self-calibration does not require *a priori* knowledge of the pinhole positions. However, we set a requirement for it because convergence of the self-calibration algorithm is greatly improved, especially with the small dither length, if the initial guess of the distortion pattern is given by the reference method using *a priori* knowledge of the pinhole positions.

3.7 Intra-pixel sensitivity

Figure 4 plots the astrometric error due to IPS as a function of the sensitivity hole position relative to the PSF centroid. The sensitivity hole is only located along the X axis for simplicity. We see a periodic profile of the astrometric error with zero error when the sensitivity hole is located either at the pixel boundary or at the pixel center. The characteristic profile is consistent with Eq. (11) in a sense that the numerator becomes small (or large) when the sensitivity hole is closer to (or farther from) the PSF centroid than the pixel center due to a monotonically decreasing PSF profile. We also see that the astrometric error is only significant when the sensitivity hole is located at a distance where the PSF profile has a steep slope. Our simulation reveals that, in the very worst case where the sensitivity hole is completely dark at its peak, the astrometric error due to IPS is ~ 8 uas peak-to-peak or a few uas rms. The IPS effect is more significant at shorter wavelengths because the PSF slope becomes steeper. It is expected to be ~ several uas at the shortest wavelength. Although the contribution is still small compared to other effects, we will consult with the detector vendor as to what causes the IPS, frequency of occurrence on the detector, and mitigation to minimize the increase in the laboratory, etc.

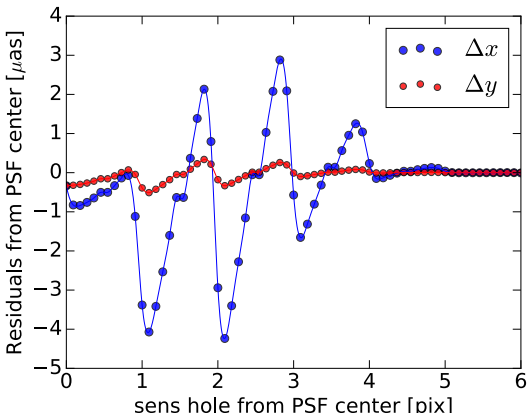

Figure 4. Astrometric error as a function of sensitivity hole position relative to the PSF centroid. The blue and red dot and line represent the error along x-axis, and y-axis, respectively. The sensitivity hole is only moved along the x axis.

3.8 Pixel Size Irregularity

Figure 5 shows the required pinhole grid interval as a function of PSI when the astrometric error allocation to PSI (σ_{PSI} in Eq. (13)) is 4 uas. We see a trend that the pinhole grid interval increases as the PSI becomes smaller. Since the current distortion correction plan indicates that the pinhole grid interval is ~ 64 pix after taking into account the dither length of 200 pix, PSI shall be as small as 10^{-3} of a pixel.

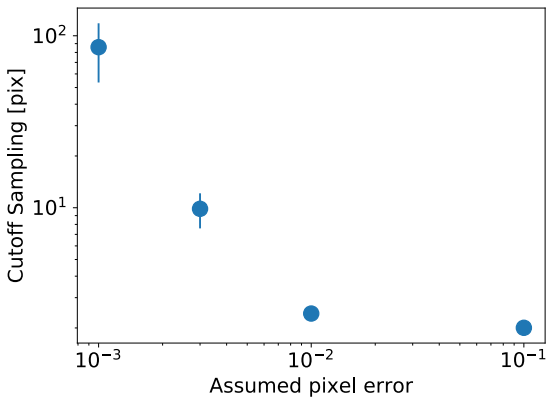

Figure 5. The minimum required pinhole grid interval on the vertical axis as a function of PSI on the horizontal axis. The minimum pinhole grid interval shown here is specifically for $\sigma_{PSI} = 4$ uas in Eq. (13).

4. SUMMARY

We have described formulation, data, and results of our analyses performed to flow down allocations in the astrometry error budget to specific requirements to components, calibration plan, operation plan, and data reduction plan. The analyses covered in this paper are specifically related to atmospheric dispersion, optical distortion, and detector characteristics. The requirements generated out of this paper are summarized in Table 2. This paper, combined with other similar existing and upcoming documentations forms the basis of the requirement flow down and supports the astrometry error budget to ensure that TMT/NFIRAOS/IRIS, when they are built, will achieve the astrometry goals as planned.

REFERENCES

[1] Larkin, J. et al., "The Infrared Imaging Spectrograph (IRIS) for TMT: instrument overview," Proc. SPIE 9908, (2016).

[2] Herriot, G. et al., "NFIRAOS: first facility AO system for the Thirty Meter Telescope," Proc. SPIE 9148, (2014).

[3] Fritz, T., Gillessen, S., Trippe, S., Ott, T., Bartko, H., Pfuhl, O., Dodds-Eden, K., Davies, R., Eisenhauer, F., Genzel, R., "What is limiting near-infrared astrometry in the Galactic Centre?," MNRAS, 401, 1177 (2010).

[4] Yelda, S., Lu, J. R., Ghez, A. M., Clarkson, W., Anderson, J., Do, T., Matthews, K., "Improving Galactic Center Astrometry by Reducing the Effects of Geometric Distortion," ApJ, 725, 331 (2010).

[5] Schöck, M., Do, T., Ellerbroek, B. L., Gilles, L., Herriot, G., Meyer, L., Suzuki, R., Wang, L., Yelda, S., "Thirty Meter Telescope astrometry error budget," Proc. SPIE 9148, (2014).

[6] Schöck, M., Andersen, D., Rogers, J., Ellerbroek, B., Chisholm, E., Dunn, J., Herriot, G., Larkin, J., Moore, A., Suzuki, R., Wincentsen, J., Wright, S., "Flowdown of the TMT astrometry error budget(s) to the IRIS design," Proc. SPIE, 9908, (2016)

[7] Rayner, J. T., Cushing, M. C., Vacca, W. D., "The Infrared Telescope Facility (IRTF) Spectral Library: Cool Stars," ApJS, 185, 289 (2009).

[8] Kurucz, R. L., CD-ROM No. 13, ATLAS9 Stellar Atmosphere Programs and 2 km/s Grid (1993).

[9] Phillips, A. C., Bauman, B. J., Larkin, J. E., Moore, A. M., Niehaus, C. N., Crampton, D., Simard, L., "he Infrared Imaging Spectrograph (IRIS) for TMT: the atmospheric dispersion corrector," Proc. SPIE 7735, (2010).

[10] Suzuki, R., "Distortion correction of NFIRAOS and IRIS," TMT technical report, TMT.INS.TEC.17.181.DRF01 (2017).
[11] Hardy, T., Willot, C., Pazder, J., "Intra-pixel response of the new JWST infrared detector arrays," Proc. SPIE 9154, (2014).
[12] Hohenkerk, C. Y. & Sinclair, A. T., "The Computation of Angular Atmospheric Refraction at Large Zenith Angles," NAO Technical Note 63, HM Nautical Almanac Office (1985).
[13] Suzuki, R., "High Precision Measurement of Atmospheric Dispersion," TMT technical report, TMT.AOS.TEC.14.070.DRF01 (2014).